Supporting Information

Tailoring Crystallization Dynamics and Phase Evolution of Co-evaporated Pure α-$FAPbI_3$ for Enhanced Device Performance

Francesca Zarotti[1,4], Erica Magliano[2,4], Suresh Podapangi[1], Federico Trezzini[1], Elham Ghavidel[1], Venanzio Raglione[2], Marco Di Giovannantonio[2], Francesco Di Giacomo[1,b], Alessandro Coati[3], Roberto Felici[2], and Aldo Di Carlo[1,2,*]*

[1]C.H.O.S.E. (Center for Hybrid and Organic Solar Energy), Electronic Engineering Department, University of Rome Tor Vergata, Via del Politecnico 1, 00118, Rome, Italy.

[2]Istituto di Struttura della Materia (CNR-ISM) National Research Council, via del Fosso del Cavaliere 100, 00133, Rome, Italy.

[3]Synchrotron SOLEIL, L'Orme des Merisiers, Saint-Aubin, 91192 Gif sur Yvette, France

[4]Both authors contributed equally to this work.

AUTHOR INFORMATION

Present addresses:

[a] ENEA, Italian National Agency for New Technologies, Energy and Sustainable Economic Development, Via Enrico Fermi, 45, 00044 Frascati, Rome, Italy.

[b] Solertix S.r.l., Via Eusebio Chini 15, 00147, Rome, Italy.

CORRESPONDING AUTHORS:

- Francesca Zarotti, francesca.zarotti@uniroma2.it
- Aldo Di Carlo, aldo.dicarlo@uniroma2.it

The temperatures of FAI source employed in literature span a relatively broad range, approximately from 150 °C to 250 °C.[1–6] However, different studies identify different upper temperature limits for the thermal stability of FAI. For example, Kroll *et al.* suggest not exceeding approximately 195 °C[4], whereas Petry *et al.* indicate that temperatures in the range of 220–240 °C should be avoided[3].

We believe that these discrepancies likely arise from differences in the experimental setups, particularly from the positioning of the thermocouple and the resulting uncertainty in the actual temperature applied to the material. As a result, nominally similar temperature values may correspond to different effective thermal conditions across different systems.

In our setup, we experimentally observe that the crucible temperature should not exceed approximately 220 °C, as above this threshold the FAI shows visible changes in appearance, becoming slightly brownish and exhibiting early signs of carbonization.

The FAI sublimation temperature was maintained at 210 °C to avoid thermal degradation, which became evident above 220 °C through brown discoloration of the powder. To further investigate this decomposition, we performed ^{1}H-NMR measurements on FAI evaporated at 210 °C and 240 °C (i.e., beyond the nominal identified "safe" temperature of 220 °C). FAI powders collected from different processes were weighed (30 mg) and dissolved in 0.6 mL of DMSO-d_6. The final concentration of the analyzed samples was 50 mg mL^{-1}, corresponding to 0.29 M. Among the analyzed samples, the powder collected from the conical crucible after evaporation at 240 °C appeared darker in color, as shown in Figure S1-a.

The spectra show a progressive broadening of the –NH_2 resonance at comparable –CH signal intensities with the increasing evaporation temperature (Figure S1-b,c). The spectrum of the pristine FAI powder is also included for reference.

Contrary to previous reports, under our experimental conditions the thermal evaporation of FAI does not result in severe degradation or significant hydroiodic acid (HI) formation. This is evidenced by the absence of splitting of the –NH proton signal, which would be expected in the presence of HI, as observed by Feeney T. *et al.* for high-rate processes, and by Petry J. *et al* for high-temperature depositions.[3,7] While minor chemical modifications are suggested by the progressive –NH_2 peak broadening, no evidence of substantial FAI decomposition or HI formation is observed in our case.

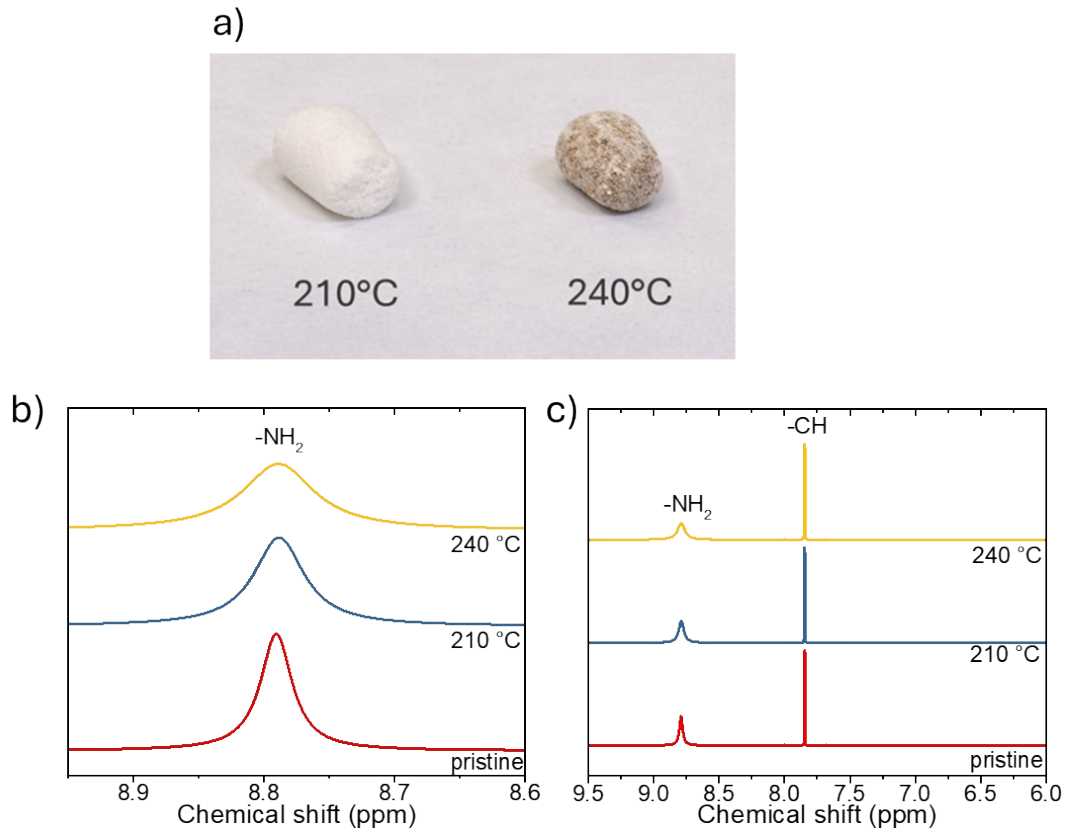

Figure S1: a) Residual FAI material after thermal evaporation at 210 °C and 240 °C, respectively. b-c) ^{1}H-NMR spectra of residual FAI material for increasing sublimation temperatures (210 and 240 °C) and of the pristine FAI powder used for deposition, with a zoom in -NH_2 range in b, showing a progressive peak broadening with increasing sublimation temperature.

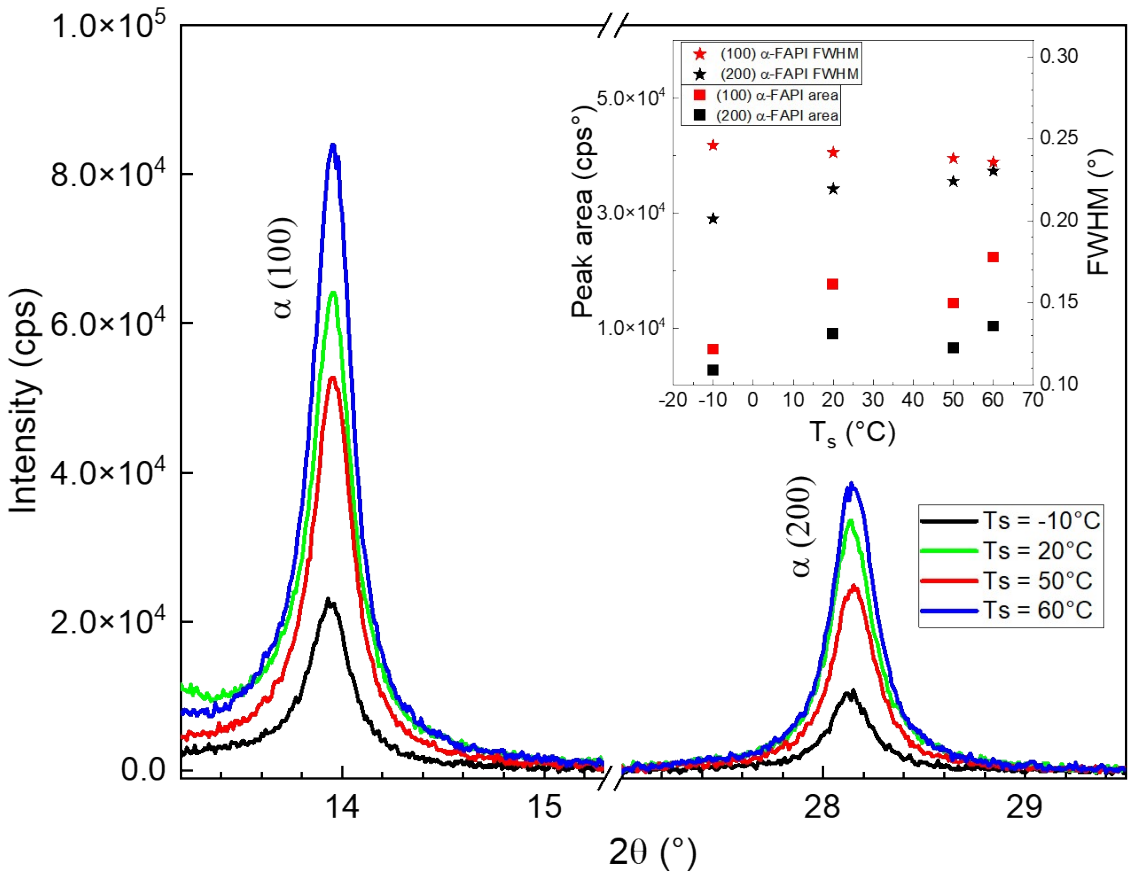

Figure S2: XRD intensity of the (100) and (200) reflections of α-phase $FAPbI_3$ perovskite films as a function of substrate temperature (T_s), based on 120 min co-depositions at a fixed FAI source temperature of 200 °C and PbI_2 source temperature of 345°C. The inset shows the evolution of peak area and full width at half maximum (FWHM) for both reflections across the investigated substrate temperatures.

The continuous 200-minute $FAPbI_3$ evaporation process, without any FAI substitution or modification during vacuum deposition, shows a clear presence of δ-phase (Figure S3) and a subsequent annealing step at 150°C for 15 min is required to promote the transition to black α-phase (Figure S3). Also the perovskite morphology is affected by the annealing step (Figure S4). Prior to annealing, the films exhibit a heterogeneous morphology characterized by an amorphous region, along with the presence of large, rounded grains approximately 500 nm in size, with a similar morphology already shown by Roß *et al.*[8] The annealed film exhibits a more homogeneous morphology, with an average grain size of approximately 350 nm. Larger grains reach sizes up to 520 nm, while smaller grains, likely originating from the transformation of previously amorphous regions, are around 180 nm in diameter.

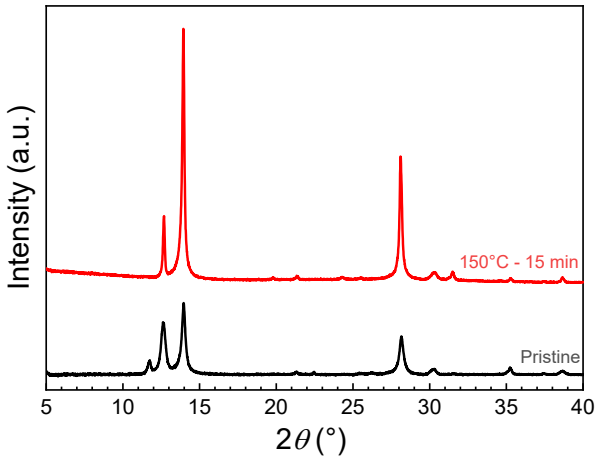

Figure S3: XRD spectra of glass/ITO/PTAA/continuous 200-minute $FAPbI_3$, before (pristine, black curve) and after (150°C - 15 min, red curve) the annealing step.

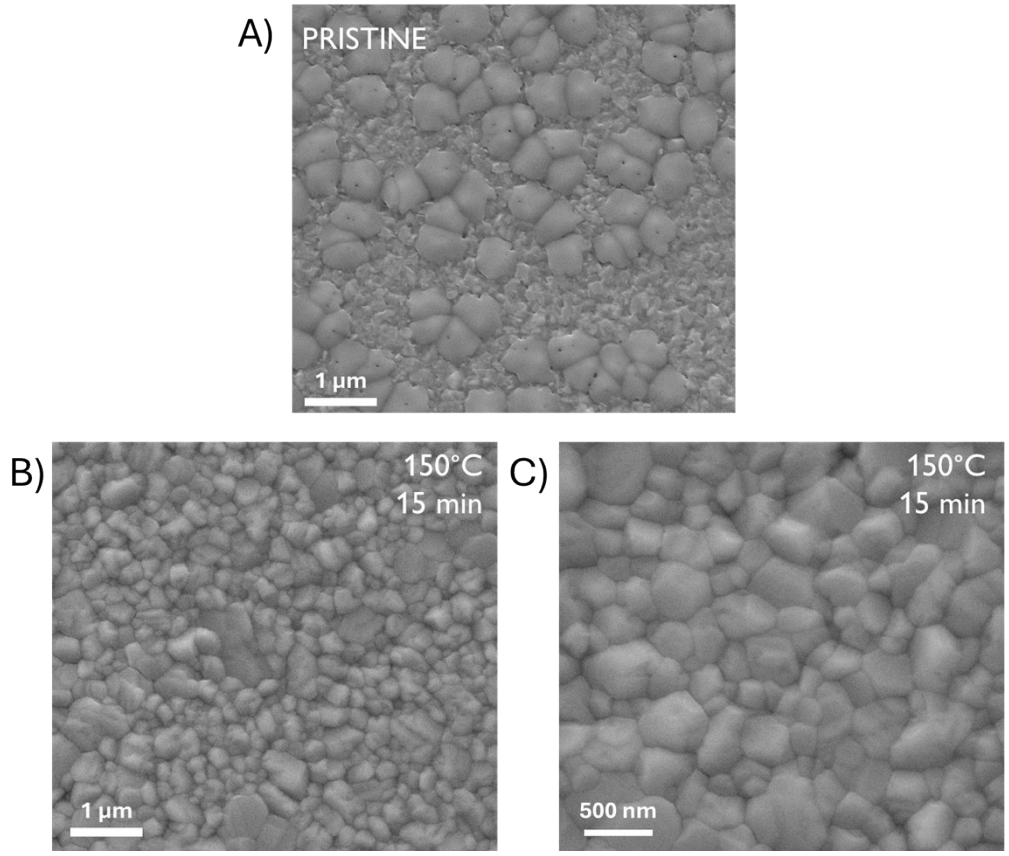

Figure S4: Top-view SEM images of continuous 200 minute $FAPbI_3$ layer on glass/ITO/PTAA, before (A) and after (B,C) the annealing step.

The stability of the Continuous-200 and Type-200 perovskite films was evaluated by XRD after exposing both samples to ambient air (Figure S5). In the Continuous-200 case (Figure S5-a), a pronounced PbI_2 peak is already present, indicating residual PbI_2 and incomplete conversion. Upon air exposure, two additional reflections gradually emerge at 9.9° and 11.7° and increase in intensity over time. The reflection at 11.7° is attributed to the formation of the δ-phase, while the low-angle peak at 9.9° can be assigned either to a lamellar FA–Pb–I intermediate phase (d ≈ 8.9 Å) or to the reported one-dimensional FA_3PbI_5 compound, which has been observed in the literature under FAI-rich conditions.[9,10]

These results indicate that air exposure induces partial decomposition of α-$FAPbI_3$ into PbI_2 and δ-phase, accompanied by the formation of a low-angle intermediate phase, as evidenced by the appearance of the 9.9° reflection and its higher-order harmonics. After 760 h, the δ-phase peak becomes predominant.

In contrast, optimized Type-200 film (Figure S5-b) exhibits only minor formation of the δ-phase upon air exposure within 40 hours, with no detectable low-angle reflections. This suggests that the perovskite framework remains largely intact, suppressing FA segregation and preventing the formation of intermediate lamellar phases. After 760 h, the intensity of the δ-phase peak increases, while the α-phase remains the dominant orientation.

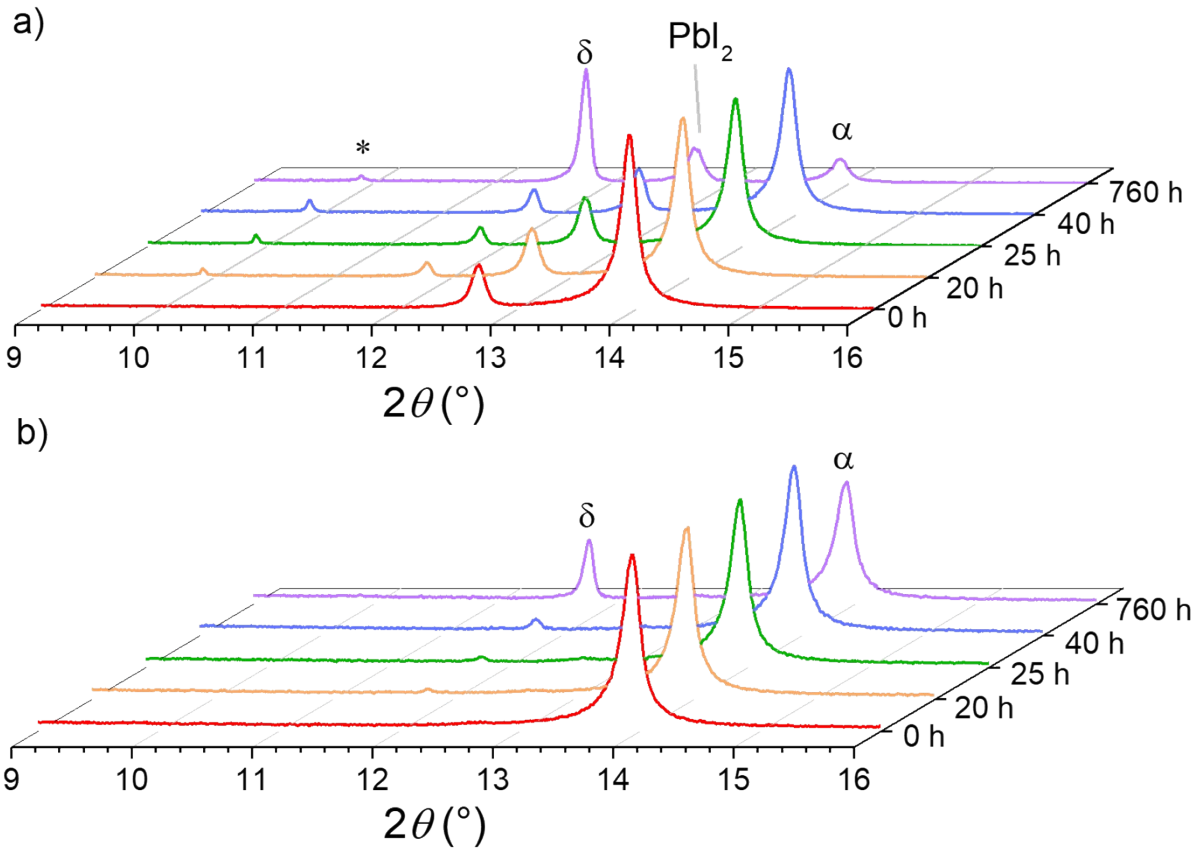

Figure S5: Time evolution of the XRD patterns of Continuous-200 (a) and Type-200 (b) perovskite films deposited on glass/ITO/PTAA, and exposed to ambient air for up to 760 h.

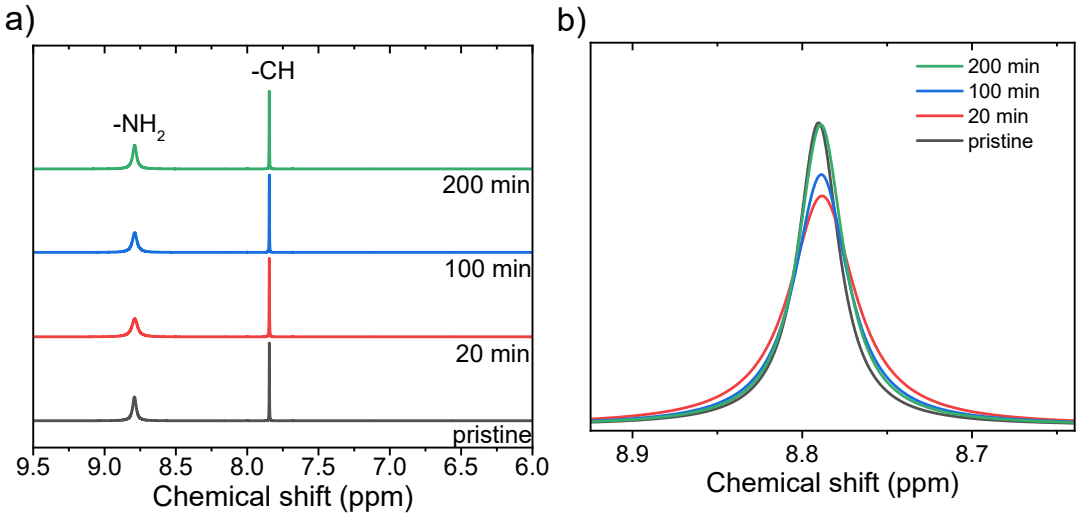

Figure S6: ^{1}H-NMR spectra of pristine FAI powder (black curve) used for thermal evaporation, residual FAI powder from crucible after 20 (red curve), 100 (blue curve), 200 (green curve) minutes of evaporation. In b), expanded view of the ^{1}H NMR spectra highlighting the –NH_2 proton region.

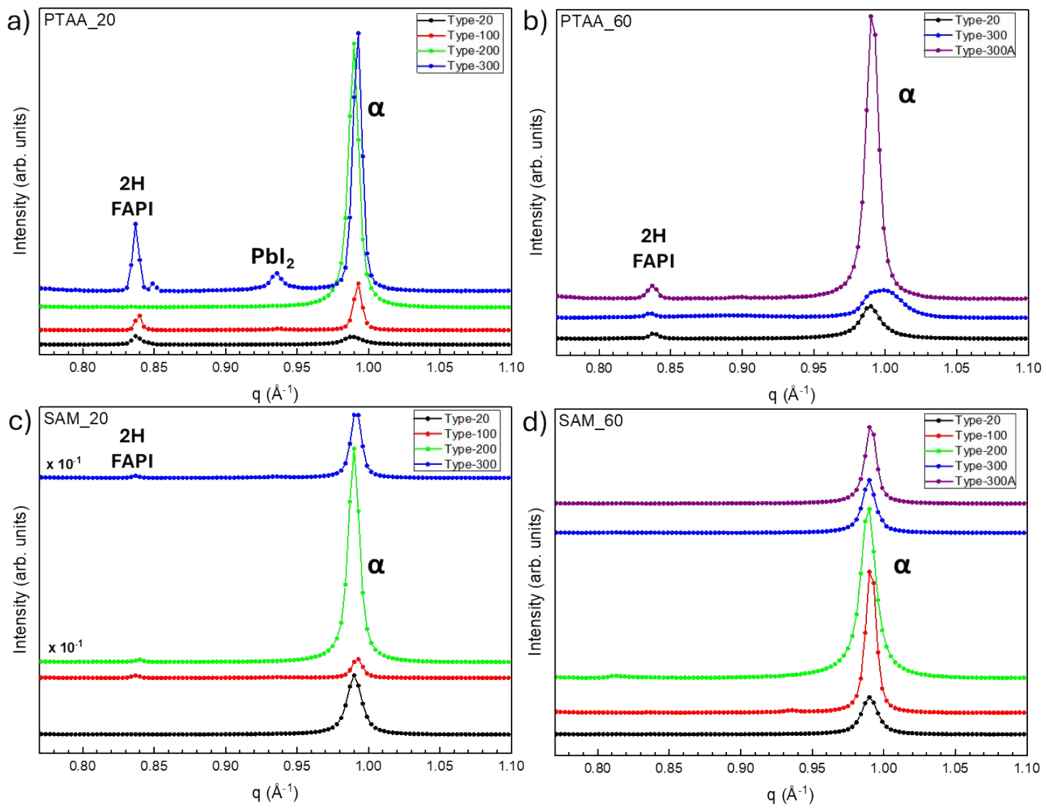

Figure S7: Zoomed view of Figure 2 of the manuscript, focusing on the q-range between 0.77 Å⁻¹ and 1.10 Å⁻¹. In plot a), for the Type-300, two low-intensity peaks are observed at q ≈ 0.85 Å⁻¹ and q ≈ 0.93 Å⁻¹, corresponding to distortions in the δ-phase (100) and (001) reflections of PbI_2, respectively. These features likely originate from either partial degradation of the sample or defects introduced during the deposition process.

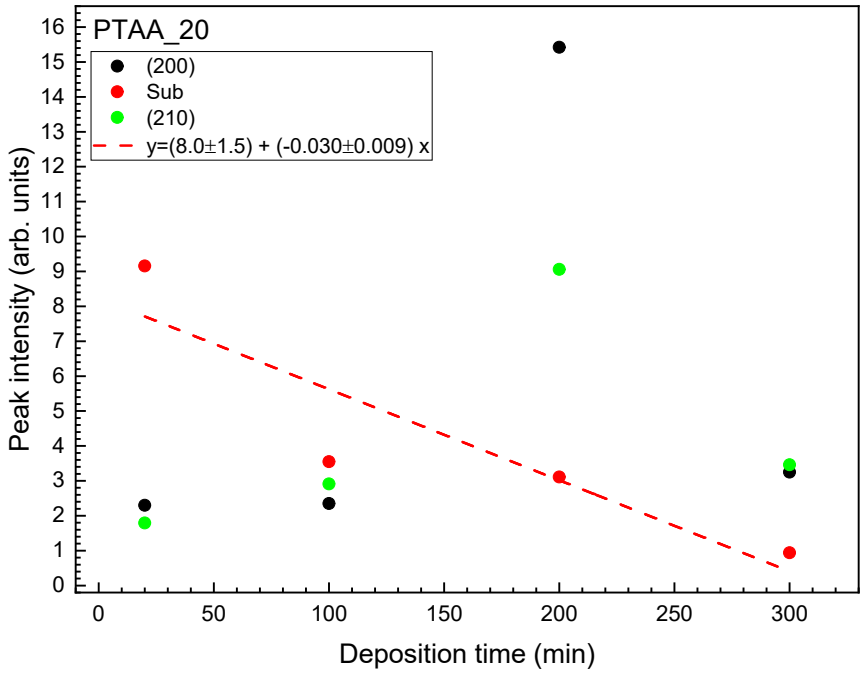

Figure S8: Peak intensities of the α-phase (200) and (210) reflections, shown alongside the most intense substrate peak at q ≈ 2.15 Å $^{-1}$, as a function of growth time for the PTAA20 samples.

Texture of the samples:

Figure S9 shows the distribution of α-phase reflections, normalized to the most intense peak of the α-series for each sample. It can be observed that both PTAA and SAM samples exhibit the same type of reflections. Notably, in all samples, the most intense reflections are (100) and (200). However, a key difference is observed: in PTAA_60, the (200) reflection is consistently the most intense, whereas in PTAA_20, this trend is only evident for the thinner perovskite layer. In the case of SAM as the HTL, the (100) reflection is always the most intense, with an inversion favoring (200) occurring only in Type-300A. Respective plots for the δ phase are shown in Figure S9 – e,f: in this case, a clear pattern is not discernible, likely due to its formation not only during deposition but also as a result of post-deposition degradation.

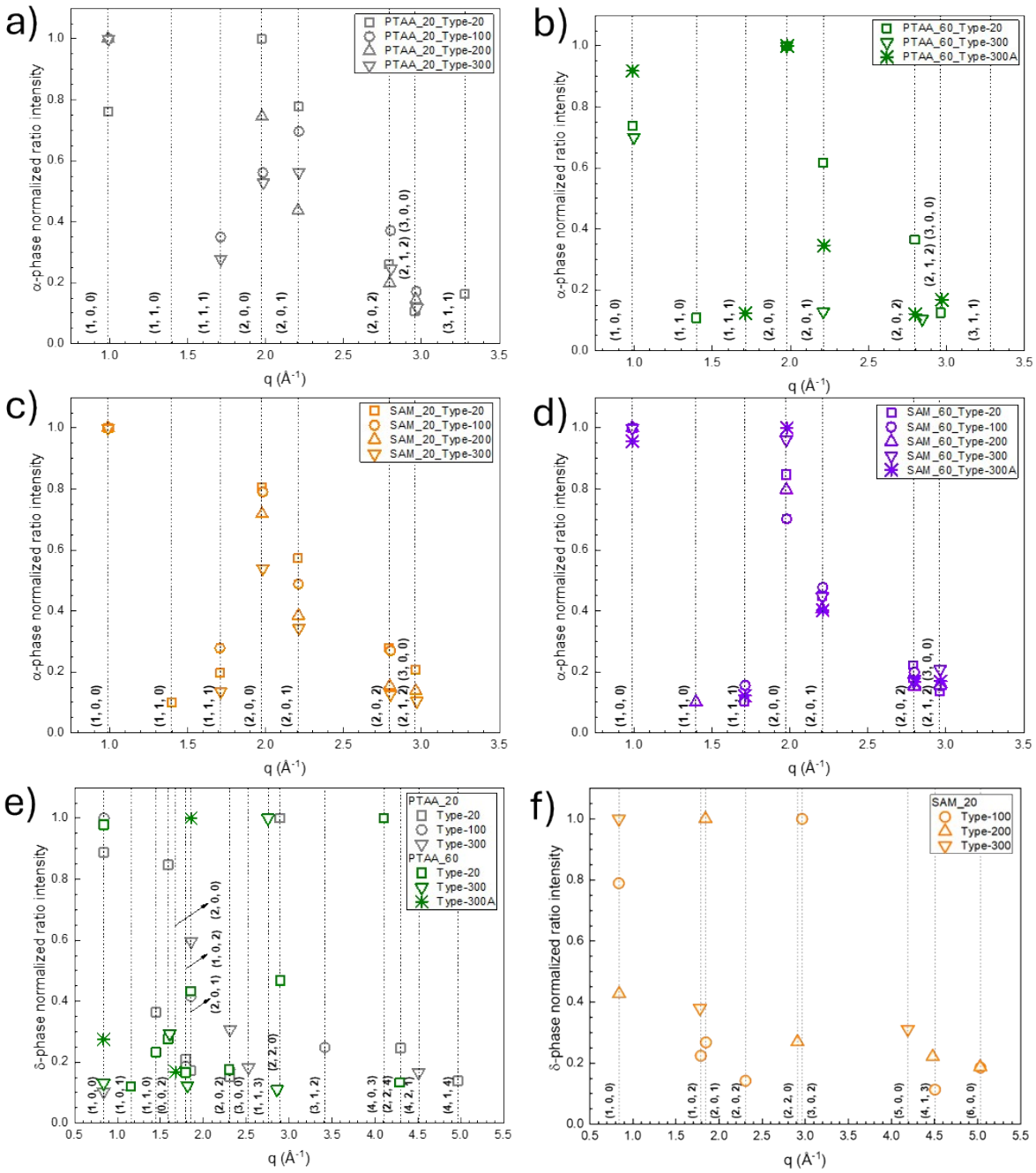

Figure S9: Ratio of α-phase peak intensities, normalized to the most intense α-phase reflection, for $FAPbI_3$ films deposited on PTAA at substrate temperatures of a) 20 °C and b) 60 °C, and on SAM at c) 20 °C and d) 60 °C. Intensity ratios of δ-phase reflections, normalized to the most intense δ-phase peak, are shown for e) PTAA20 and PTAA60, and for f) SAM20. Data for SAM60 are omitted since no δ-phase was detected. The corresponding (hkl) indices are indicated for each data point.

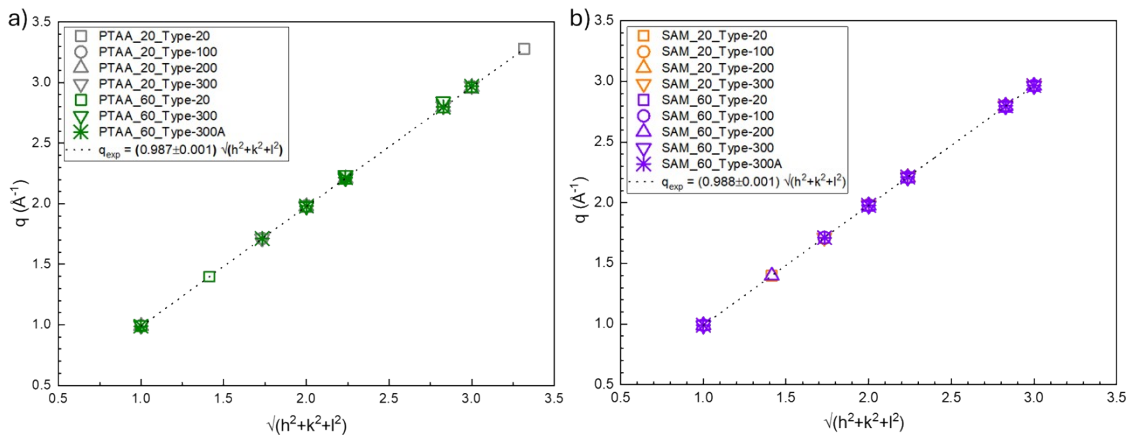

Figure S10: Plots of momentum transfer (q) versus √(h² + k² + l²) for reflections attributed to the α-phase in PTAA and SAM samples, along with the corresponding linear fit.

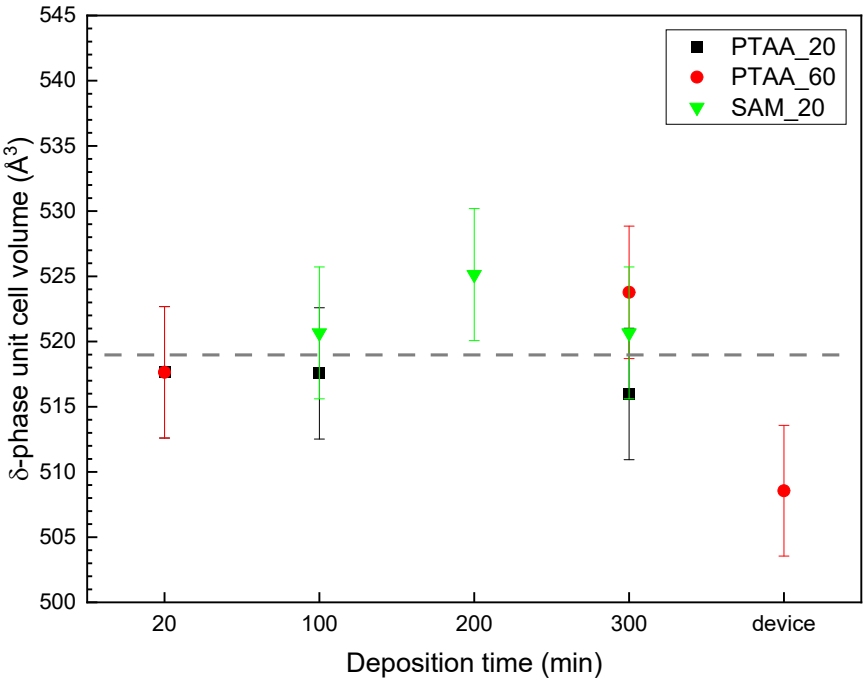

Figure S11: Unit cell volume of the δ-phase as a function of deposition time for SAM and PTAA samples. SAM_60 is excluded as no δ-phase was detected under those conditions. The grey dashed line indicates the average unit cell volume.

(h, k, l)	**q ($Å^{-1}$)**	**2θ (°) [λ_{Cu}= 1.54 Å]**	**phase**
(1, 0, 0)	0,84	11,78	δ-phase
(1, 0, 0)	0,99	13,94	α-phase
(1, 0, 1)	1,16	16,28	δ-phase
(1, 1, 0)	1,40	19,77	α-phase
(1, 1, 0)	1,45	20,47	δ-phase
	1,52	21,48	Substrate (glass/ITO)
(0, 0, 2)	1,59	22,44	δ-phase
(2, 0, 0)	1,68	23,73	δ-phase
(1, 1, 1)	1,71	24,21	α-phase
(1, 0, 2)	1,79	25,41	δ-phase
(2, 0, 1)	1,85	26,24	δ-phase
(2, 0, 0)	1,97	27,96	α-phase
	2,15	30,57	Substrate (glass/ITO)
(2, 0, 1)	2,21	31,44	α-phase
(2, 0, 2)	2,30	32,82	δ-phase
	2,48	35,41	Substrate (glass/ITO)
(3, 0, 0)	2,53	36,08	δ-phase
	2,63	37,62	Substrate (glass/ITO)
(1, 1, 3)	2,75	39,47	δ-phase
(2, 0, 2)	2,79	40,01	α-phase
(2, 2, 0)	2,90	41,58	δ-phase
(2, 1, 2)	2,96	42,56	α-phase
(3, 0, 0)	2,96	42,56	α-phase
	3,17	45,74	Substrate (glass/ITO)
(3, 1, 1)	3,28	47,43	α-phase
(3, 1, 2)	3,42	49,54	δ-phase
	3,51	50,98	Substrate (glass/ITO)
	3,63	52,86	Substrate (glass/ITO)
	3,83	56,02	Substrate (glass/ITO)
	4,03	59,22	Substrate (glass/ITO)
(4, 0, 3)	4,10	60,42	δ-phase
	4,12	60,68	Substrate (glass/ITO)
	4,21	62,15	Substrate (glass/ITO)
(2, 2, 4)	4,30	63,57	δ-phase
(4, 2, 1)	4,51	67,13	δ-phase
	4,56	67,99	Substrate (glass/ITO)
(4, 1, 4)	4,97	75,00	δ-phase

Table S1: Correspondence between Miller indices (h, k, l), scattering vector q, and 2θ values, calculated using Cu Kα radiation (λ = 1.54 Å). Each q value is associated with its corresponding crystalline phase or substrate.

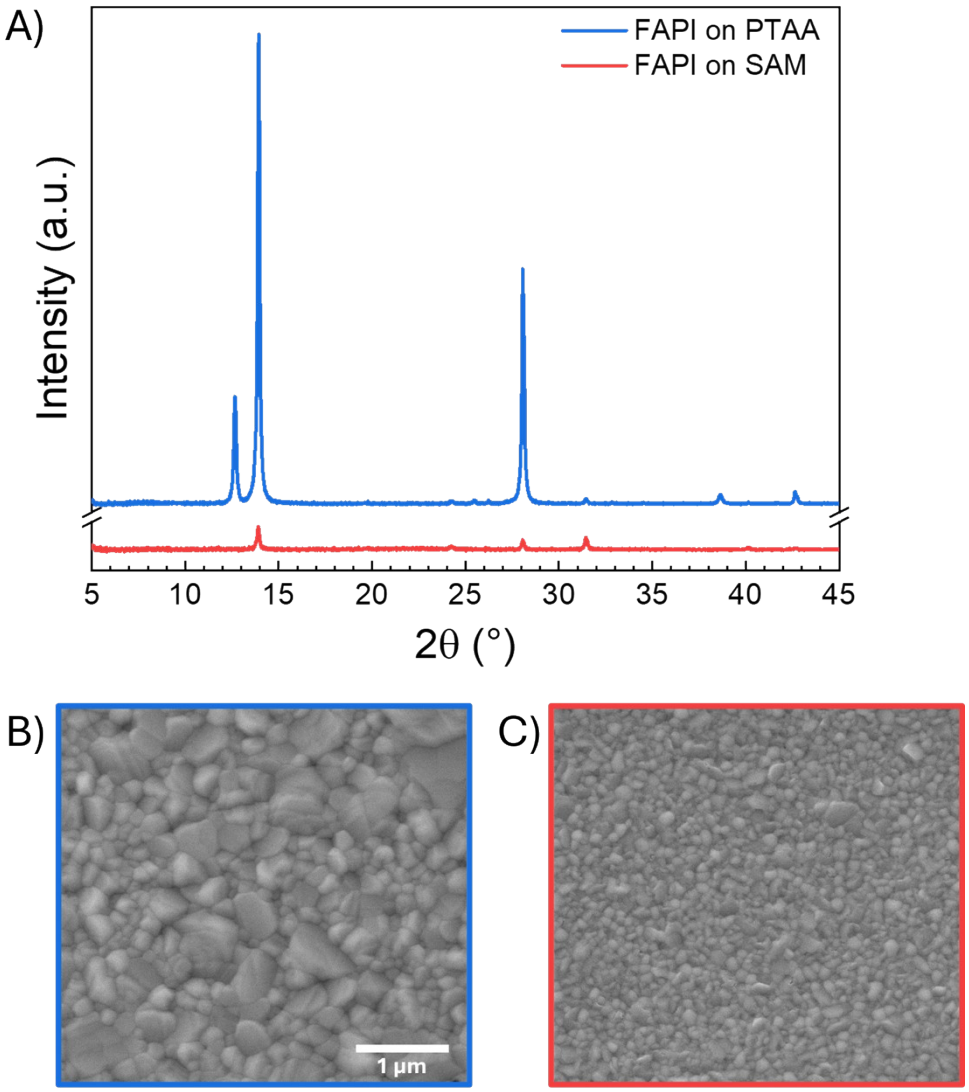

Figure S12: A) XRD pattern of FAPI (200 min, continuous deposition) on PTAA (blue curve) and SAM (red curve). The respective morphologies are shown in the SEM images in B) and C).

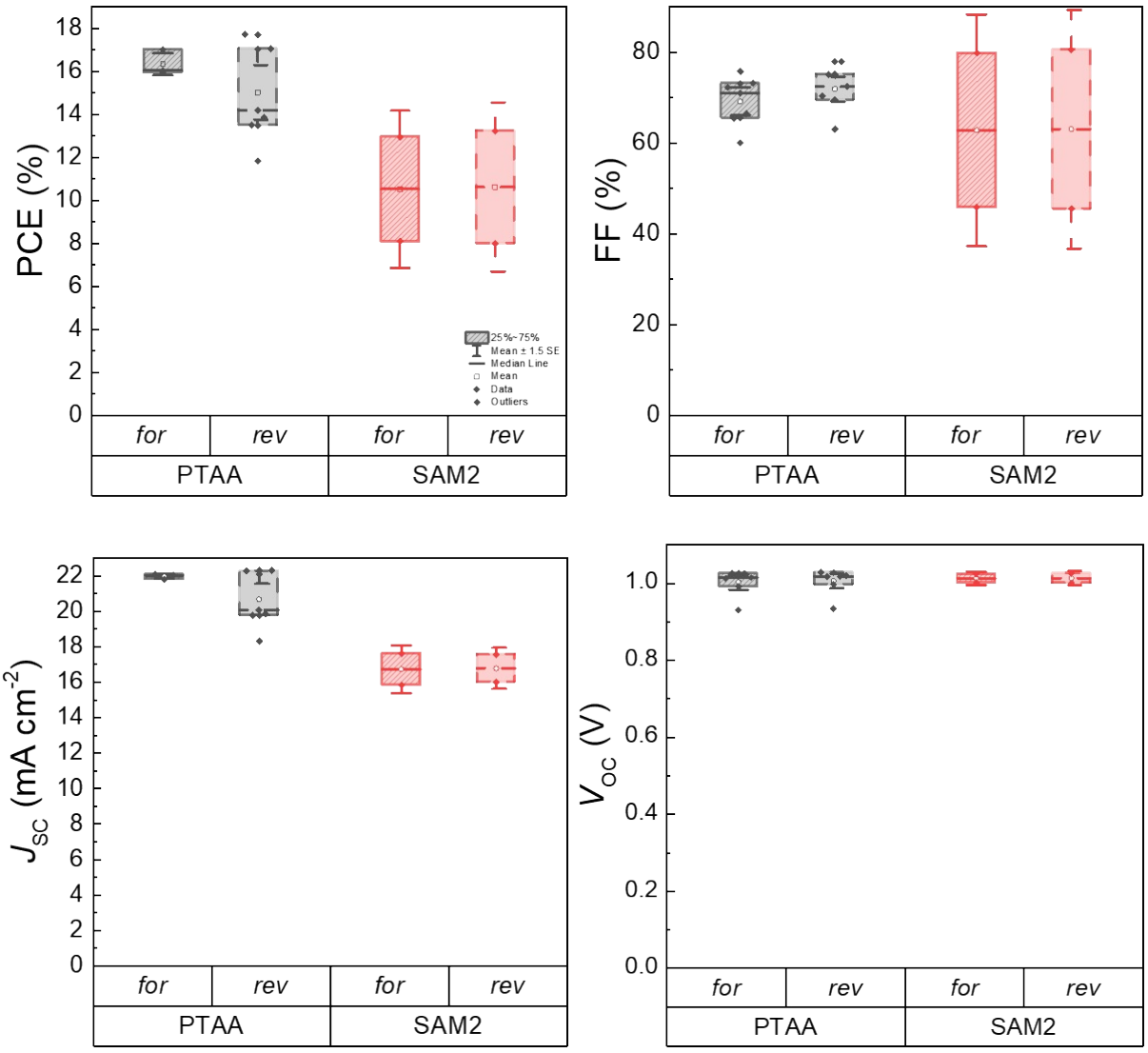

Figure S13: Statistical trends of photovoltaic parameters (PCE, FF, J_{SC}, V_{OC}) of the p-i-n devices based on PTAA (black box) or SAM (red box), from the same batch, in forward and reverse scans.

We fabricated Type-200 perovskite on both PTAA and washed SAM substrates. The SAM washing procedure was performed as reported by Feeney T. *et al.*[7] XRD analysis (Figure S14-a) indicates that, in both cases, crystal growth is predominantly oriented along the (100) direction, with enhanced intensity on PTAA. Moreover, in the case of the washed SAM, a significantly enhanced (210) reflection is observed, which may suggest a more pronounced columnar growth morphology, in agreement with previous reports in the literature.[11,12] In contrast, films deposited on PTAA exhibit a more ordered and stoichiometric crystalline structure under the same deposition conditions. Top-view SEM analysis (Figure S14-b) further supports these findings, showing the presence of smaller grains in the washed SAM- based samples.

This reduced film quality correlates with the observed device performance, where a reduced J_{SC} is measured for the washed SAM devices (Figure S15). Consistently, EQE measurements also confirm a lower charge collection efficiency across the spectral range.

As compared to SAM-based substrates, while the orientation appears similar, the reproducibility is enhanced when introducing the washing.

We further corroborate that PTAA behaves as a more chemically inert HTL. As a result, the composition deposited during evaporation is largely preserved at the substrate interface, leading to minimal perturbation of the intended stoichiometry.

In contrast, SAM and washed SAM substrates appear to induce stronger interactions during growth, which may affect the final film formation. In one case, the presence of phosphonic acid functional groups is enhancing FAI adsorption and preventing delta-phase formation. On the other hand, the washing step can enhance process reproducibility but more FAI can be required, as observed in previous works.[7,8]

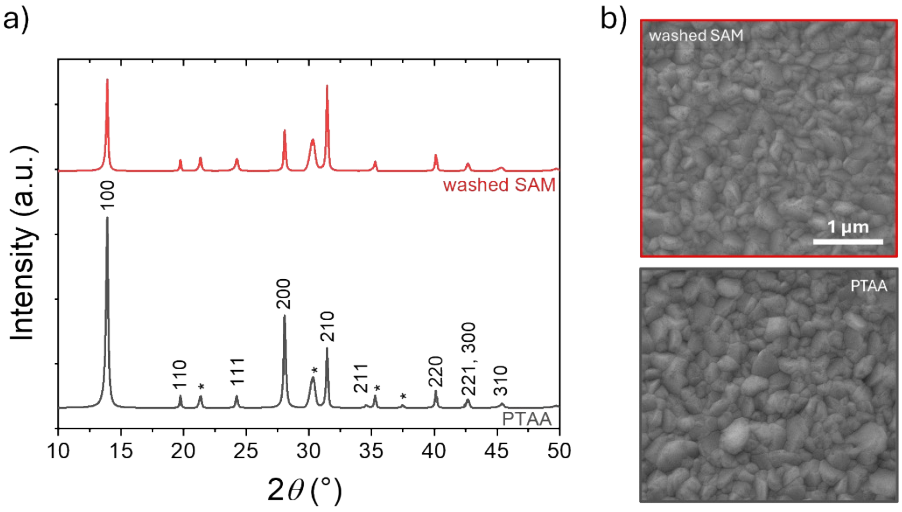

Figure S14: a) XRD patterns and b) top-view SEM images of Type-200 perovskite films grown on washed SAM (red) and PTAA (black). In the XRD patterns, the ITO peaks of the underlying substrate are indicated with the asterisks (*).

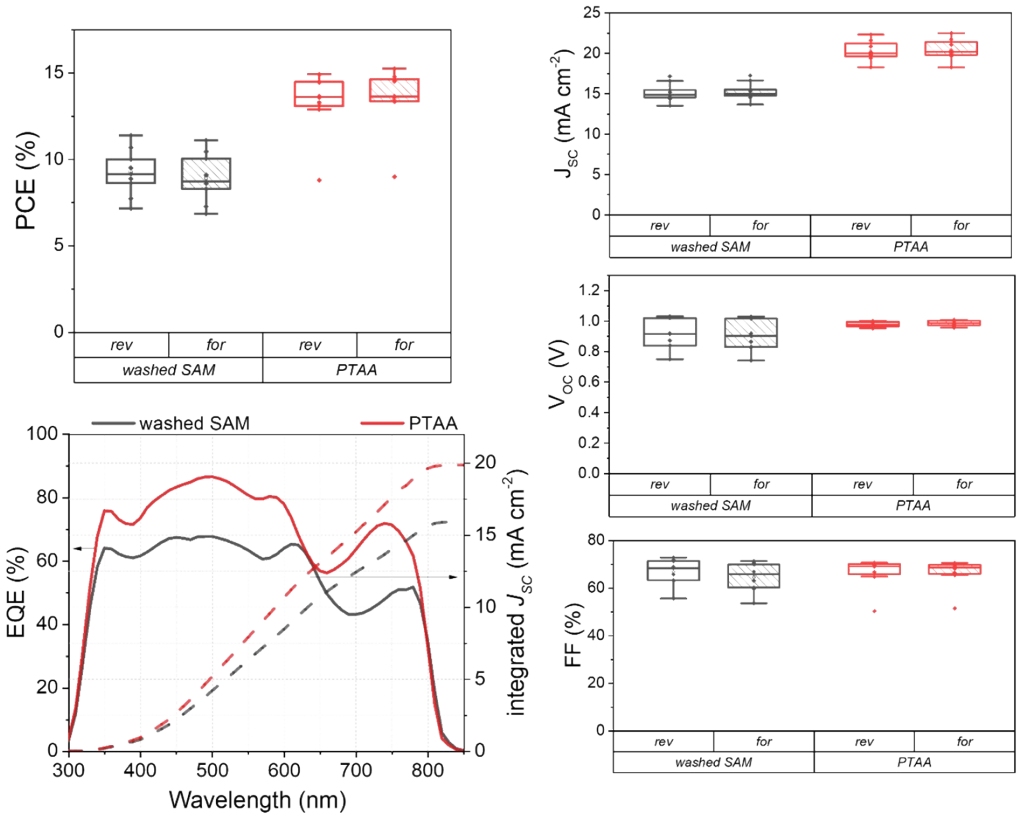

Figure S15: Box plots of the electrical parameters and EQE of the devices fabricated on washed SAM (black) and PTAA (red).

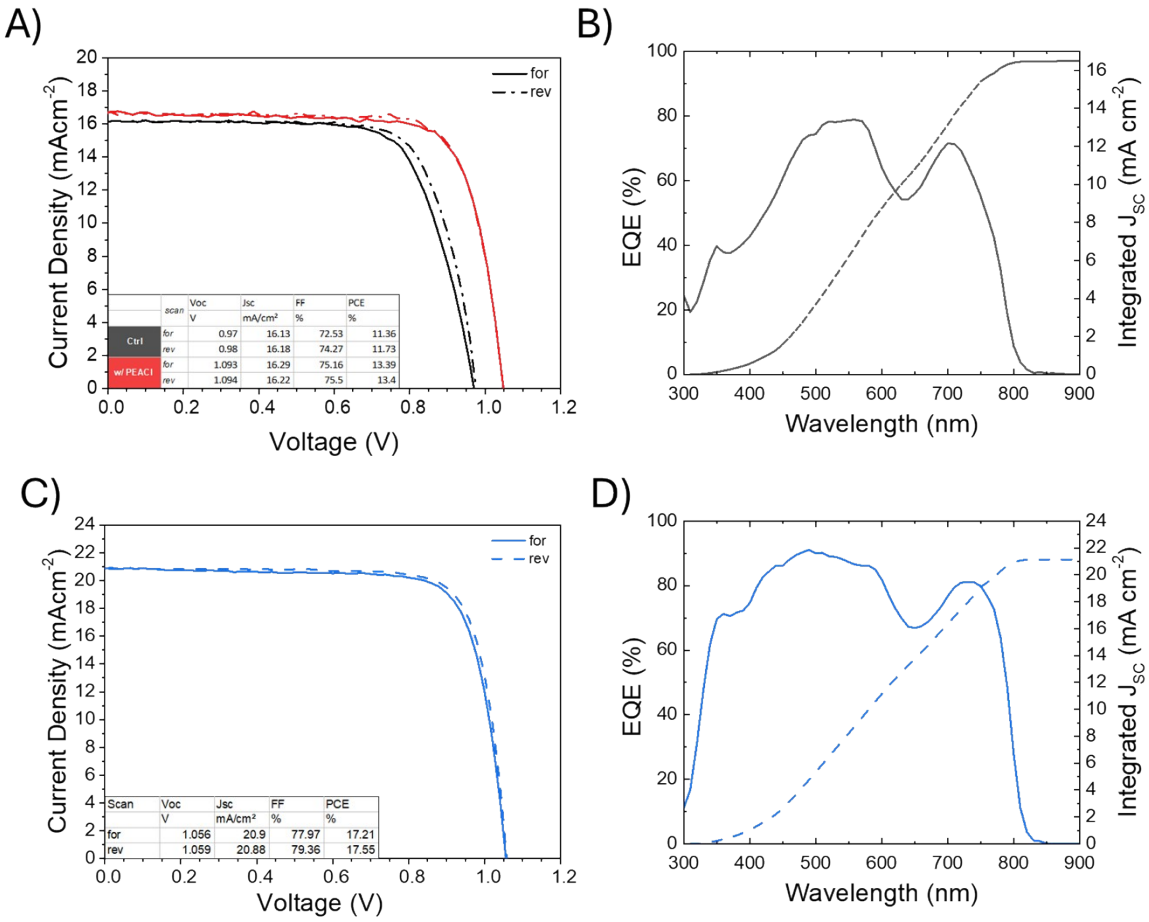

Figure S16: A) Current density-voltage (J-V) characteristic of p-i-n devices based on FAPI co-evaporation of 200 min without FAI replacement, with (Ctrl - black curve) and without PEACl (w/ PEACl - red curve). C) J-V of Type-200 FAPI-based p-i-n device. In the tables, the electrical parameters of the characteristics are reported. The EQE plot of the Ctrl device is reported in B), whereas the EQE of Type-200 FAPI-based device is reported D).

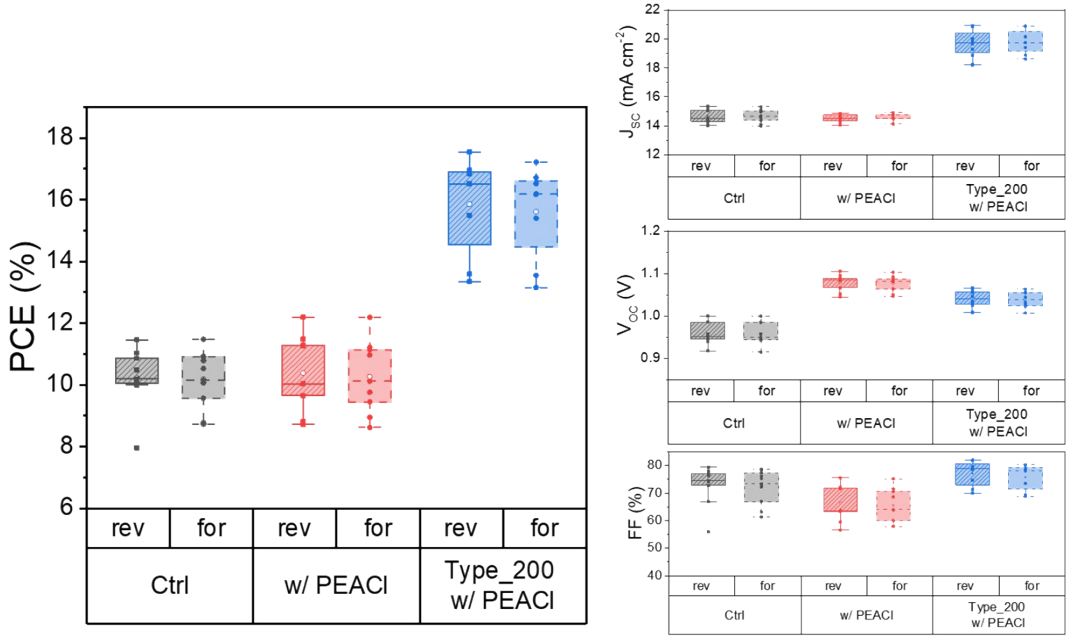

Figure S17: PCE, J_{SC}, V_{OC} and FF box plots of p-i-n devices based on FAPI deposited continuously for 200 min, without (Ctrl – black box) and with PEACl (w/ PEACl – red box), and of Type-200 FAPI-based devices with PEACl passivation (Type-200 w/ PEACl -blue box).

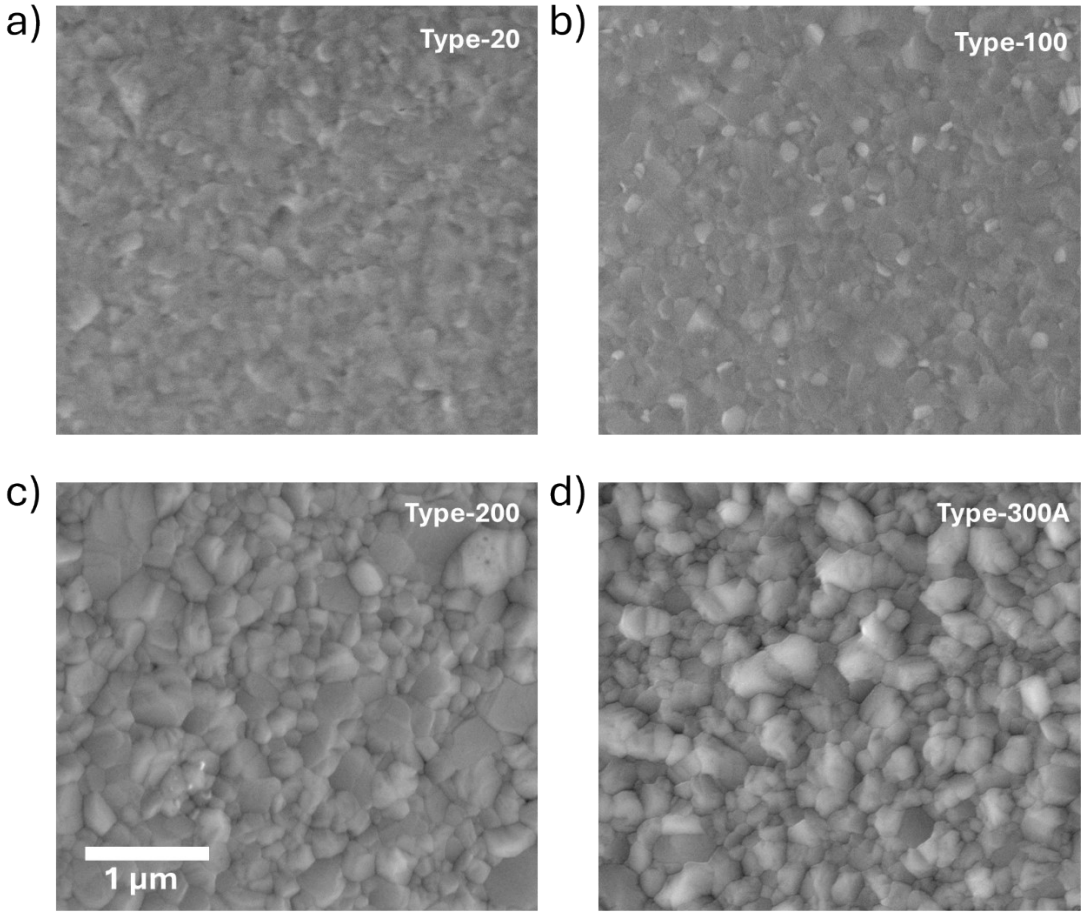

Figure S18: Top-view SEM images illustrating the progressive growth of FAPI on PTAA following the protocols described in the manuscript (a) Type-20, b) Type-100, c) Type-200, and d) Type-300A), showing the evolution of the grain coarsening during perovskite growth.

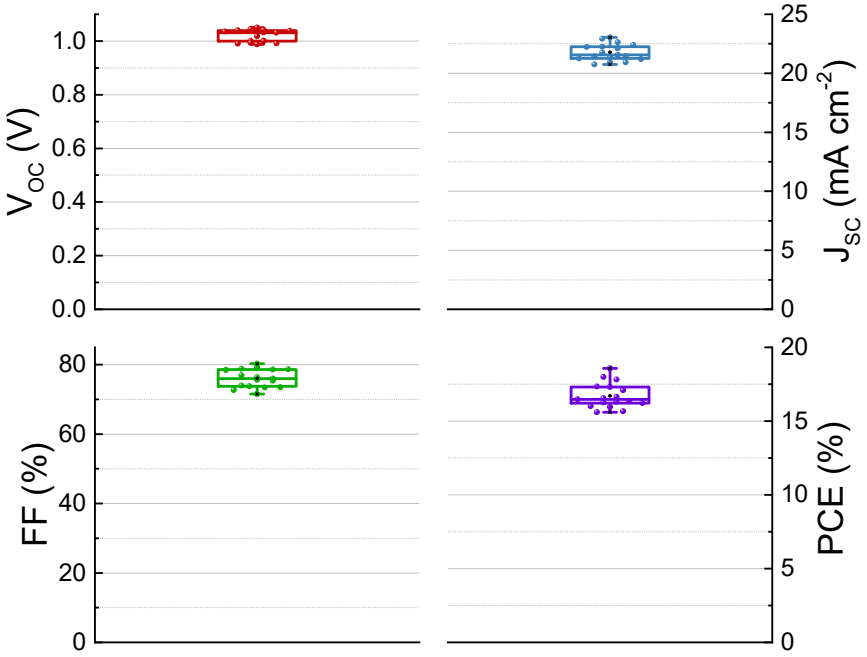

Figure S19: Electrical parameters (V_{OC}, J_{SC}, FF and PCE) distribution from one batch of Type-300A-based devices.

Table S2: Summary of reported device parameters for co-evaporated $FAPbI_3$-based solar cells, including both pure and additive-containing compositions.

Year	Additives	Architecture	Bandgap (eV)	V_{OC} (V)	J_{SC} (mA cm^{-2})	FF (%)	PCE (%)	Area (cm^2)	Ref
2017	pure FAPI	nip	1.55	1.01	22.1	70.8	15.8	0.0919	[1]
2017	pure FAPI	nip	1.55	n.a.	17	n.a.	14.2	64	[1]
2021	pure FAPI	pin	1.54	1.08	21.2	74.11	16	0.16	[8]
2025	pure FAPI	pin	1.53	1.1	20.3	71	15	0.118	[13]
2021	47% MAI	pin	1.53	1.05	25.7	75.91	20.4	0.16	[8]
2021	32% MAI	pin	1.53	1.05	23.2	74.86	18.2	0.16	[8]
2023	Cs, Cl, seed layer (PbI_2)	pin	1.59	1.06	22.8	82	19.8	0.25	[14]
2024	Cs, Cl	pin	1.58	1.069	20.6	77	17	0.105	[7]
2024	Cs, Br, seed layer (CsCl)	pin	1.65	1.2	20.6	80	19.6	0.16	[15]
2025	Cs, Br	pin	1.67	1.14	19.7	81	18.1	0.0825	[16]
2025	Cs, Br	pin	1.58	1.09	21.3	75	17.5	0.172	[17]
2025	*pure FAPI*	*pin*	*1.54*	*1.04*	*22.63*	*78.61*	*18.5*	*0.09*	*This work*

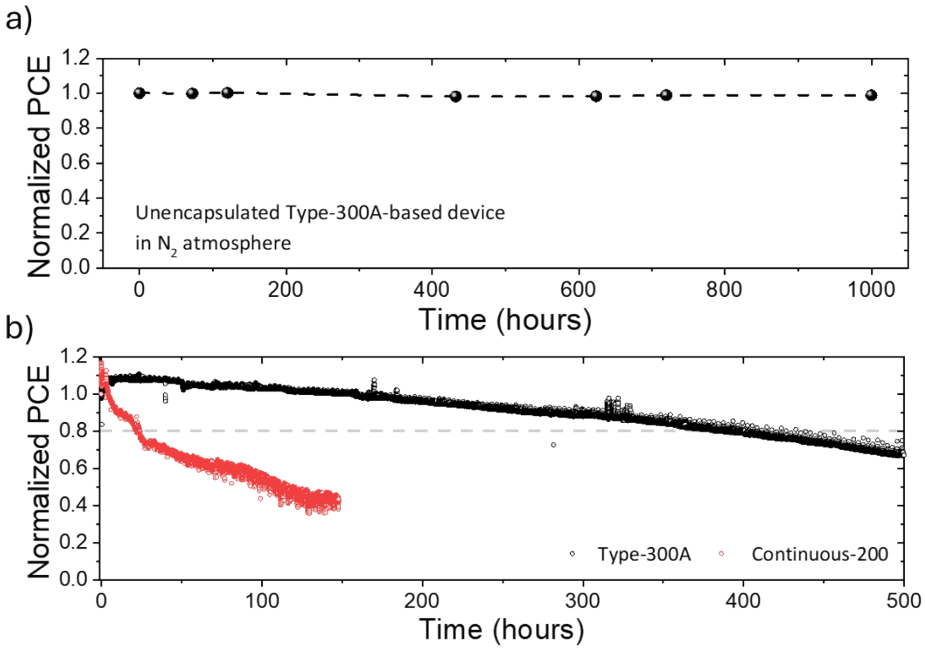

Figure S20: Normalized PCE evolution under shelf-life and ISOS-L1 stability tests. a) Shelf-life stability of unencapsulated Type-300A-based device stored under inert atmosphere (N_2 glovebox) and measured in ambient air. b) ISOS-L1 of encapsulated Type-300A (black curve) and Continuous-200-based (red curve) devices.

Continuous-300 Process:

Devices fabricated using Continuous-300 process for FAPI co-evaporation exhibited poor performance, mainly due to a significantly reduced J_{SC}, as also shown from the EQE response (Figure S19).

XRD analysis (Figure S20-a) reveals a low intensity of the α-phase perovskite peaks, along with the presence of the δ-phase, and a preferred orientation deviating from the typical (100), instead showing a dominant contribution along (210).

Cross-sectional SEM analysis (Figure S20-b) reveals a perovskite thickness of approximately 475 nm. However, the film exhibits poor morphology: although a predominantly columnar growth is observed, smaller and irregular grains are present throughout the structure. This is also contributing to the observed low device performance.

This experiment is further strengthening and supporting our thesis. Extended continuous deposition promotes the formation of increasingly disordered perovskite structures, which negatively impacts film quality and device performance. In contrast, the introduction of intermediate annealing steps in our approach plays a key role in reshaping a quasi-ordered structure for the subsequently deposited overlayer, thereby improving structural coherence and overall film quality. Additionally, continuous evaporation over extended durations (i.e., higher then 100 minutes) leads to significant limitations, primarily due to the progressive physical and chemical changes of FAI under prolonged thermal stress.

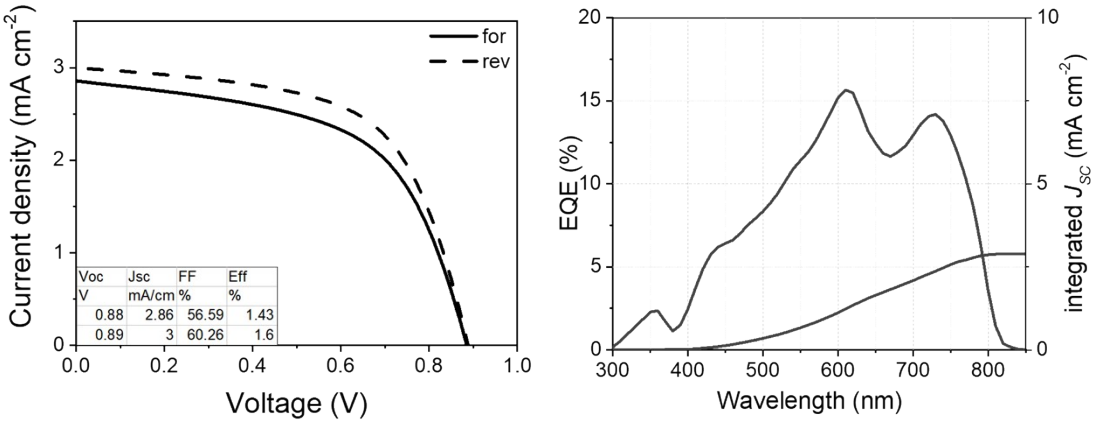

Figure S21: J-V (left) and EQE (right) of p-i-n devices with the following stack: glass/ITO/PTAA/Continuous-300 Perovskite/PEACl/PCBM/BCP/Cu.

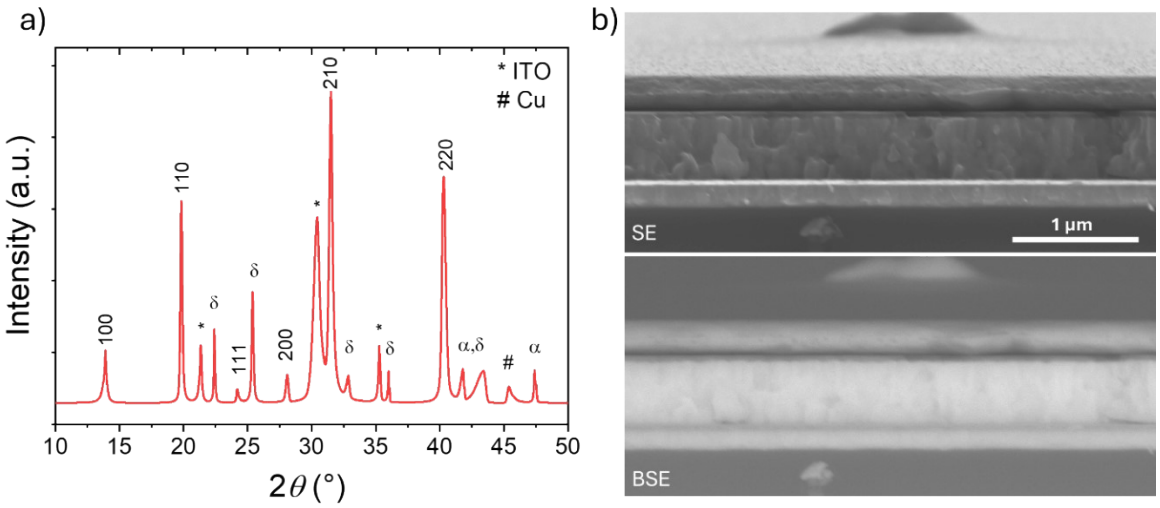

Figure S22: a) XRD pattern and b) cross-sectional SE and BSE images of a device based on Continuous-300 perovskite process.

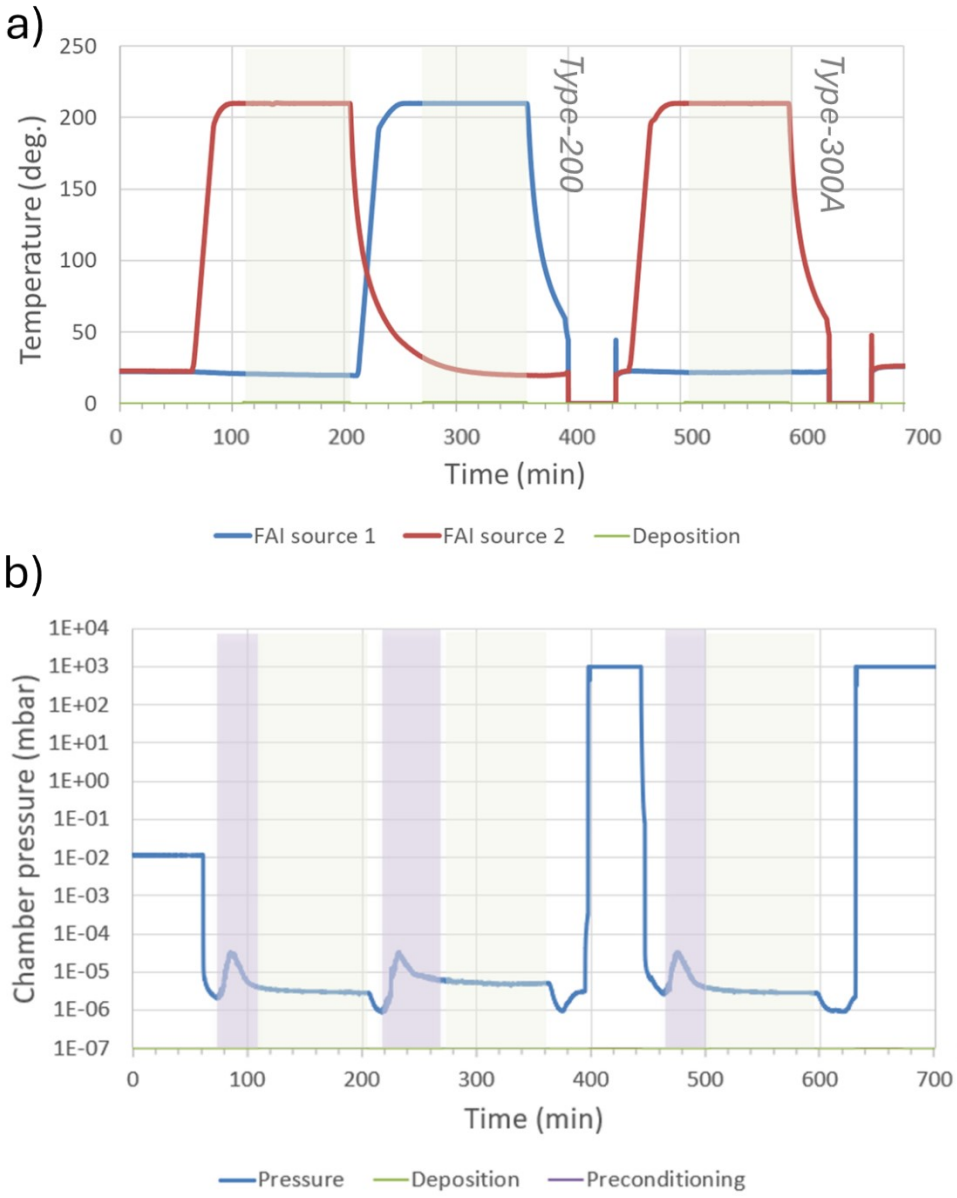

Figure S23: a) Temperature evolution of the FAI sources during the Type-200 (up to ~360 min) and Type-300A (up to 600 min) deposition processes. Two different FAI sources are sequentially employed for the Type-200 process (red and blue curves) without breaking vacuum, while a third source is loaded for the Type-300A deposition process. The substrate shutter is opened for 100 min, as indicated by the green shaded area. b) Chamber pressure as a function of time. During the preconditioning step, the shutter is kept closed and a pressure bump, attributed to the outgassing of degradation products, is observed (purple shaded area).

BIBLIOGRAPHY

1. Borchert, J. *et al.* Large-Area, Highly Uniform Evaporated Formamidinium Lead Triiodide Thin Films for Solar Cells. *ACS Energy Lett.* **2**, 2799–2804 (2017).

2. Gil-Escrig, L. *et al.* Vacuum Deposited Triple-Cation Mixed-Halide Perovskite Solar Cells. *Adv. Energy Mater.* **8**, 1–6 (2018).

3. Petry, J. *et al.* Industrialization of perovskite solar cell fabrication: strategies to achieve high-throughput vapor deposition processes. *EES Sol.* **1**, 404–418 (2025).

4. Kroll, M. *et al.* Insights into the evaporation behaviour of FAI: material degradation and consequences for perovskite solar cells. *Sustain. Energy Fuels* (2022) doi:10.1039/d2se00373b.

5. Li, H. *et al.* Sequential vacuum-evaporated perovskite solar cells with more than 24% efficiency. *Sci. Adv.* **8**, (2022).

6. Chiang, Y.-H., Anaya, M. & Stranks, S. D. Multisource Vacuum Deposition of Methylammonium-Free Perovskite Solar Cells. *ACS Energy Lett.* **5**, 2498–2504 (2020).

7. Feeney, T. *et al.* Understanding and exploiting interfacial interactions between phosphonic acid functional groups and co-evaporated perovskites. *Matter* **7**, 2066–2090 (2024).

8. Roß, M. *et al.* Co-Evaporated Formamidinium Lead Iodide Based Perovskites with 1000 h Constant Stability for Fully Textured Monolithic Perovskite/Silicon Tandem Solar Cells. *Adv. Energy Mater.* **11**, (2021).

9. Leyden, M. R., Lee, M. V., Raga, S. R. & Qi, Y. Large formamidinium lead trihalide perovskite solar cells using chemical vapor deposition with high reproducibility and tunable chlorine concentrations. *J. Mater. Chem. A* **3**, 16097–16103 (2015).

10. Ma, F. *et al.* Stable α/δ phase junction of formamidinium lead iodide perovskites for enhanced near-infrared emission. *Chem. Sci.* **8**, 800–805 (2017).

11. Abzieher, T. *et al.* From Groundwork to Efficient Solar Cells: On the Importance of the Substrate Material in Co-Evaporated Perovskite Solar Cells. *Adv. Funct. Mater.* **31**, (2021).

12. Roß, M. *et al.* Co-Evaporated p-i-n Perovskite Solar Cells beyond 20% Efficiency: Impact of Substrate Temperature and Hole-Transport Layer. *ACS Appl. Mater. Interfaces* **12**, 39261–39272 (2020).

13. Yang, T. C.-J. *et al.* Incorporating thermal co-evaporation in current-matched all-perovskite triple-junction solar cells. *EES Sol.* **1**, 41–55 (2025).

14. Yan, S. *et al.* A Templating Approach to Controlling the Growth of Coevaporated Halide Perovskites. *ACS Energy Lett.* **8**, 4008–4015 (2023).

15. Škorjanc, V. *et al.* Seed Layers for Wide-Band Gap Coevaporated Perovskite Solar Cells: CsCl Regulates Band Gap and Reduces Process Variability. *ACS Energy Lett.* **9**, 5639–5646 (2024).

16. Gil-Escrig, L. *et al.* Tuning substrate temperature for enhanced vacuum-deposited wide-bandgap perovskite solar cells: insights from morphology, charge transport, and drift-diffusion simulations. *EES Sol.* **1**, 391–403 (2025).

17. Feeney, T. *et al.* High-Rate FA-Based Co-Evaporated Perovskites: Understanding Rate Limitations and Practical Considerations to Overcome Their Impact. *Adv. Funct. Mater.* **17873**, 1–14 (2025).